

Localized Electrochemical Deposition of Porous Cu-Ni Microcolumns: Insights into the Growth Mechanisms and the Mechanical Performance

E. Pellicer^{1,}, S. Pané², V. Panagiotopoulou², S. Fusco², K. M. Sivaraman², S. Suriñach¹, M. D. Baró¹, B. J. Nelson² and J. Sort³*

¹ Departament de Física, Facultat de Ciències, Universitat Autònoma de Barcelona, E-08193 Bellaterra, Spain

² Institute of Robotics and Intelligent Systems (IRIS), ETH Zürich, CH-8092 Zürich, Switzerland

³ Institució Catalana de Recerca i Estudis Avançats (ICREA) and Departament de Física, Universitat Autònoma de Barcelona, E-08193 Bellaterra, Spain

*E-mail: eva.pellicer.icn@uab.cat

Received: 22 March 2012 / *Accepted:* 14 April 2012 / *Published:* 1 May 2012

Cu-rich Cu-Ni alloy microcolumns (11-35 at% Ni) with large porosity degree were grown by localized electrochemical deposition (LECD) at voltages of 6.5 and 7.0 V. In turn, conventional electrodeposition was used to deposit fully-compact Cu-Ni films with analogous Ni/Cu ratios from a similar citrate-containing electrolytic solution. The localized supply rate of the predominant Cu(II) and Ni(II) electroactive species in the LECD microregion was calculated assuming both large and small concentration gradients. A shortage of Cu(II) at the cathode surface is mainly responsible for the development of porosity in the microcolumns, which directly affects mechanical performance, specifically nanoindentation hardness and Young's modulus. From nanoindentation experiments, a relative microcolumn density ranging between 14 and 20% was determined. These values indicate the current efficiency of the LECD process and can be used to calculate the consumption rates associated with metal cation electroreduction.

Keywords: localized electrochemical deposition; Cu-Ni alloy; porosity; nanoindentation; hardness

1. INTRODUCTION

Porous metal structures are receiving considerable attention because of the unique combination of the finest qualities of metals and the properties of porous materials. Porous metals are characterized by their light weight, permeability, large surface area, absorbability of mechanical impacts, and heat dissipation, amongst others, which has promoted their use in several technological applications such as

filtering systems, liquid storage, orthopaedic tools or heat exchangers [1]. Various manufacturing processes including foaming, powder sintering, fiber sintering, metal injecting molding, dealloying and electrodeposition are used to produce porous metals with varying porosity degree, pore size and interconnectivity [2-5]. Electrodeposition offers the advantage that porosity can be generated in-situ, i.e. during the deposition of the metallic electrodeposit without the need for secondary steps (e.g., etching or machining) often required with other processing methods. The growth of porous metallic layers of copper [6], gold [7], iridium [8] or Co-Pd alloy [9] has been demonstrated by template-free direct electrodeposition. The common feature among these efforts is the use of hydrogen co-evolution as a source of porosity.

Interestingly, the growth of micron-sized features is also available through a variant of the electrodeposition technique, termed localized electrochemical deposition (LECD). To date, almost all efforts in LECD have been directed towards the growth of nonporous, highly dense micropillars, microcolumns and microhelices. However, the existence of porosity in these micron-sized 3D objects is not necessarily detrimental. For some applications, such as heat-transfer elements for micro-electrical devices, it can be even advantageous [10]. In a LECD process, a microanode is moved in an electroplating bath with respect to the cathode to allow the growth of a metallic microfeature. The deposition starts from a localized area on the cathode to grow up towards the microanode in a controlled manner.

The microanode is intermittently driven upwards, so the deposition proceeds between the gap left by the microanode and the growing metallic column. Compared to conventional (i.e., planar) electroplating, the current density and, in turn the electric field, used in LECD are much higher, and the electrical field is asymmetrically distributed due to the geometrical confinement induced by the microanode.

Therefore, electroplating variables such as stirring rate of the solution, additives, mass- and charge-transfer controlling factors, etc. can exert different effects than for conventional electroplating [11]. The growth of metallic microcolumns of single metals (Co, Ni and Cu) has been demonstrated over the last decade. Lin and co-workers have made important contributions in this respect, such as analyzing and modelling the effects of saccharine over the lateral surface finish and internal porosity of Ni microcolumns [12] and investigating the benefits of pulse plating for Cu microcolumns [13]. The LECD of metallic alloys has been less explored, mostly because controlling the co-deposition of two metals in such a process is more complicated.

We report on the preparation of porous Cu-Ni microcolumns by LECD. The properties of the microcolumns (morphology, roughness and mechanical performance) are compared with those of planar deposits with similar chemical composition. We show that the high consumption/supply ratio of metal cations in LECD determines the porosity of the microcolumns, which is virtually absent in the homologous 2D planar layers. To this end, the mass transport rates for Cu and Ni ions have been calculated using mathematical expressions previously validated both theoretically and experimentally for pure Cu and Ni microcolumns deposition and compared to the corresponding consumption rates by electrochemical reduction. Differences in porosity are a key factor influencing nanoindentation hardness and Young's modulus of the 2D and 3D Cu-Ni materials.

2. EXPERIMENTAL DETAILS

The electrodeposition of the Cu-Ni microcolumns was performed in a two-electrode configuration cell, while the Cu-Ni planar deposits were obtained in a three-electrode cell. In all cases the electrolyte contained $\text{NiSO}_4 \cdot 6\text{H}_2\text{O}$, $\text{CuSO}_4 \cdot 5\text{H}_2\text{O}$, $\text{C}_6\text{H}_8\text{O}_7 \cdot \text{H}_2\text{O}$ (citric acid monohydrate) and $\text{NaC}_{12}\text{H}_{25}\text{SO}_4$ (sodium lauryl sulfate). The analytical Ni(II)/Cu(II) molar ratio was varied between 10 and 28, while the concentration of the other reagents was not changed. A small quantity of $\text{C}_7\text{H}_5\text{NO}_3\text{SNa}$ (sodium saccharinate) was added to the bath. Analytical grade reagents and ultrapure water (18 M Ω cm) were used to prepare the solutions. The pH was set at 4.5, and the electrodeposition was performed at room temperature.

The microcolumns were grown potentiostatically on cleaned 0.5 mm-thick brass sheets (2 cm² exposed area) using a programmable Keithley 6517A power supply. Different voltages were attempted and microcolumns were found to grow well at voltages of 6.5 and 7.0 V. At lower voltages the growth rate was either too low or no microcolumn formation took place. A 3D micro-positioning system was used to manipulate the microanode with a resolution of 0.1 μm , allowing the user to set the position of the microanode and determine the size of the step and the frequency in the *xyz* axes. Details of the microanode preparation are reported elsewhere [14]. Before deposition, the microanode (175 μm of exposed diameter) was finely positioned near the brass cathode by a controlled approaching procedure. Immediately afterwards, the tip was moved upwards to a specific starting position for the deposition step. While depositing, the position of the tip was controlled by a current monitoring feedback system, and the tip was moved upwards when a programmed threshold was exceeded. The procedure was stopped when the deposition reached a desired height. The movement of the tip was executed in predefined constant steps, leaving a gap of 15 μm between the tip and the top of the microcolumn. Every time a step was completed, the new position was held and the current was once again measured and compared to the threshold until another trigger was received. The procedure continued until the deposited structure reached a specific height (around 700-800 μm).

The Cu-Ni films were grown on Cu/Ti/Si substrates (0.3 cm² exposed area) galvanostatically using a PGSTAT 120 Autolab potentiostat/galvanostat. A double junction Ag|AgCl reference electrode was used with 3 M KCl inner solution and an interchangeable outer solution made of 1 M Na_2SO_4 . A platinum sheet served as counter electrode.

The mole fractions of the species present in the bath were calculated using the MEDUSA[®] speciation software [15] for all bath components except for saccharine and sodium lauryl sulfate, since their complexing effects are negligible. The ionic strength was calculated iteratively by the program.

The morphology of films and microcolumns was characterized by scanning electron microscopy (SEM) on a Evo Zeiss operated at 20 kV and on a Merlin Zeiss operated at 4 kV, respectively. The chemical composition was determined by energy dispersive X-ray (EDX) analyses at 20 kV. The mechanical properties were evaluated using a UMIS nanoindenter from Fischer-Cripps Laboratories equipped with a Berkovich pyramidal-shaped diamond tip. The Cu-Ni films were indented on top, whilst the microcolumns were indented on the cross-section. The latter were embedded into resin and polished using diamond paste until the microcolumns cross-section was exposed to view. Nanoindentations were performed at approximately half the height of the

microcolumns. The maximum applied force was 10 mN in both cases. A load holding segment of 120 s was introduced between the load and unload segments. Proper corrections for the contact area (calibrated using a fused quartz specimen), instrument compliance, and initial penetration depth were applied. The hardness, H , and reduced elastic modulus, E_r , were derived from the load-displacement curves using the method of Oliver and Pharr [16]. From the initial slope of the unloading segment, the contact stiffness, S , was calculated as:

$$S = \frac{dP}{dh} \quad (\text{Eq. 1})$$

where P and h denote the applied load and the penetration depth during nanoindentation, respectively. The elastic modulus was evaluated based on its relationship with the contact area, A , and the contact stiffness:

$$S = \beta \frac{2}{\sqrt{\pi}} E_r \sqrt{A} \quad (\text{Eq. 2})$$

where β is a constant (King's factor) that depends on the geometry of the indenter ($\beta = 1.034$ for a Berkovich indenter) [17], and E_r is the reduced Young's modulus defined as:

$$\frac{1}{E_r} = \frac{1-\nu^2}{E} + \frac{1-\nu_i^2}{E_i} \quad (\text{Eq. 3})$$

The reduced modulus takes into account the elastic displacements that occur in the specimen with Young's modulus E and Poisson's ratio ν , and the diamond indenter tip, with elastic constants E_i and ν_i . For diamond, $E_i = 1140$ GPa and $\nu_i = 0.07$. Because of the high Young's modulus of the tip and its low Poisson's ratio, E_r is typically very similar to E for most metallic materials. Hardness can be calculated as:

$$H = \frac{P_{\text{Max}}}{A} \quad (\text{Eq. 4})$$

where P_{Max} is the maximum load applied during nanoindentation.

3. RESULTS AND DISCUSSION

Representative I-t curves associated with the growth of Cu-Ni microcolumns from a bath containing 0.7 M $\text{NiSO}_4 \cdot 6\text{H}_2\text{O}$ + 0.025 M $\text{CuSO}_4 \cdot 5\text{H}_2\text{O}$ + 0.3 M $\text{C}_6\text{H}_8\text{O}_7 \cdot \text{H}_2\text{O}$ + $8 \cdot 10^{-4}$ M $\text{NaC}_{12}\text{H}_{25}\text{SO}_4$ + $2 \cdot 10^{-3}$ M sodium saccharinate are displayed in Figure 1. At the applied voltages, the stationary currents reach values in the range between 2.2 and 2.4 mA. The resulting microcolumns are

Cu-rich and show large degrees of both internal and external porosity (Figure 2). Despite this porosity, the back-scattered electron (BSE) images confirm the formation of a Cu-Ni solid solution. This suggests that citrate is capable of bringing the reduction potentials of Cu and Ni near one another, thus favoring its co-deposition, for both conventional electrodeposition and for the LECD process. Also, the Ni/Cu ratio slightly increases along the microcolumn height (see Table 1), so that the upper part shows a larger Ni content (24 at% and 35 at% for 6.5 V and 7.0 V, respectively) than the bottom, i.e., near the brass substrate (11 at% and 20 at% for 6.5 V and 7.0 V, respectively).

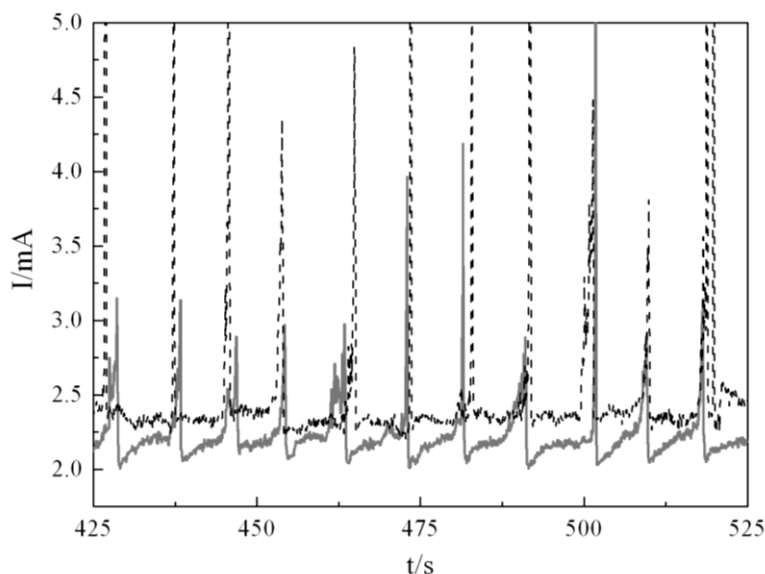


Figure 1. I-t curves (intermediate range) obtained during the LECD process from a bath containing 0.7 M $\text{NiSO}_4 \cdot 6\text{H}_2\text{O}$ + 0.025 M $\text{CuSO}_4 \cdot 5\text{H}_2\text{O}$ + 0.3 M $\text{C}_6\text{H}_8\text{O}_7 \cdot \text{H}_2\text{O}$ + $8 \cdot 10^{-4}$ M $\text{NaC}_{12}\text{H}_{25}\text{SO}_4$ + $2 \cdot 10^{-3}$ M saccharine at 6.5 V (solid grey line) and 7.0 V (dashed black line). The spikes correspond to the movement of the microanode due to the triggering signal.

Table 1. Nanoindentation hardness (H), reduced Young's modulus (E_r) and relative density ($\rho_{\text{porous}}/\rho_{\text{bulk}}$) of Cu-Ni films and microcolumns.

Applied voltage/V	Sample type	at% Ni	H / GPa	E_r / GPa	$\rho_{\text{porous}}/\rho_{\text{bulk}}$ (%)
--	Film (planar	18	4.00 ± 0.04	140.4 ± 0.3	100
--	deposit)	34	5.15 ± 0.05	160.1 ± 0.5	100
6.5	Microcolumn	11-24	0.48 ± 0.02	6.7 ± 0.4	20.5
7.0		20-35	0.72 ± 0.02	6.9 ± 0.4	19.1
6.5*		9-12	0.19 ± 0.03	3.4 ± 0.3	14.6**
7.0*		13-26	0.29 ± 0.03	3.1 ± 0.4	14.0

*saccharine-free bath

** To calculate the relative density, the E value of the planar film with 18 at% Ni has been used in Eq. 10, although the Ni content in this microcolumn and the planar film are not strictly comparable. Nevertheless, if the Young's modulus of pure bulk Cu (130 GPa) is considered instead, a value of 15.1% would be obtained, which is in any case near estimated value.

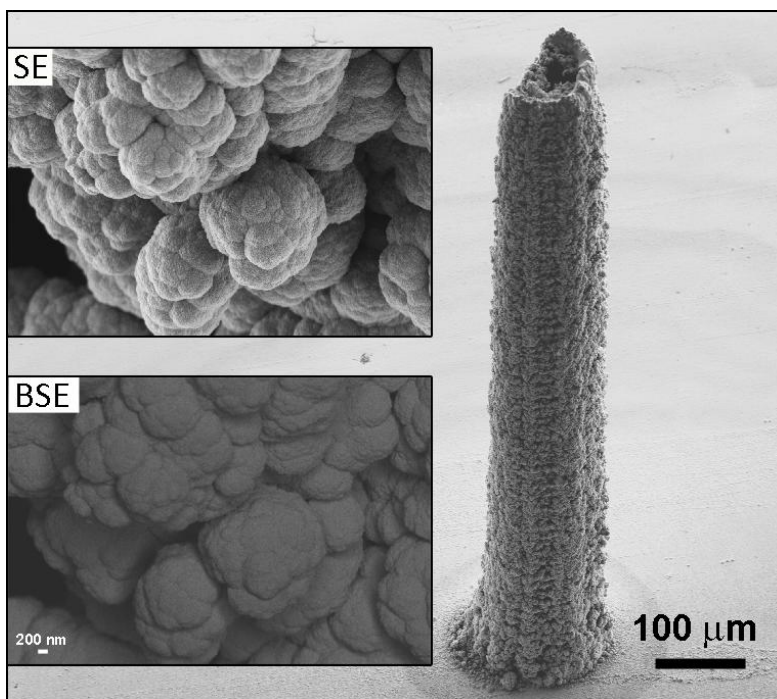


Figure 2. SEM image of the Cu-Ni microcolumn deposited at 7.0 V in the saccharine-containing bath together with secondary electron (SE) and backscattered electron (BSE) images of a zoomed detail taken at half of the height of the microcolumn.

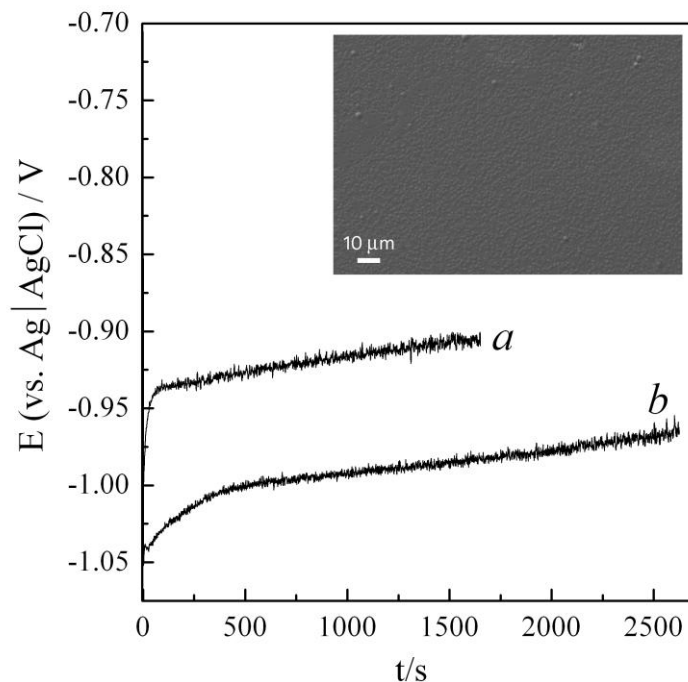


Figure 3. E-t curves for Cu-Ni film deposition onto copper-metalized silicon obtained at (a) -6.7 mA cm^{-2} from a bath containing $0.7 \text{ M NiSO}_4 \cdot 6\text{H}_2\text{O} + 0.025 \text{ M CuSO}_4 \cdot 5\text{H}_2\text{O} + 0.3 \text{ M C}_6\text{H}_8\text{O}_7 \cdot \text{H}_2\text{O} + 8 \cdot 10^{-4} \text{ M NaC}_{12}\text{H}_{25}\text{SO}_4 + 2 \cdot 10^{-3} \text{ M saccharine}$ (34 at% Ni); and (b) -13 mA cm^{-2} from a bath containing $0.66 \text{ M NiSO}_4 \cdot 6\text{H}_2\text{O} + 0.064 \text{ M CuSO}_4 \cdot 5\text{H}_2\text{O} + 0.3 \text{ M C}_6\text{H}_8\text{O}_7 \cdot \text{H}_2\text{O} + 8 \cdot 10^{-4} \text{ M NaC}_{12}\text{H}_{25}\text{SO}_4 + 2 \cdot 10^{-3} \text{ M saccharine}$ (18 at% Ni). The Ni content in the films is given in parentheses. The inset shows a SEM image of the film obtained in (a).

Although the local potential reached during microcolumn growth is unknown, the compositions suggest the occurrence of low overpotential values in which the Cu(II) species are preferentially discharged [18]. Actually, during the growth of nickel microcolumns from a sulfate bath, Lin et al. measured a local potential at the cathode of -0.64 V versus SCE when imposing a voltage of 4.6 V, in a configuration where the gap (g) between the electrodes was set to 10 μm . Taking into account the bath formulation used in this work, the applied voltages, and the value of g (15 μm), the local potentials should not be strongly negative, presumably around -0.9 V [19]. Furthermore, since the average Ni percentage in the microcolumn deposited at a voltage of 7.0 (28 at%) is higher than at 6.5 V (18 at%), larger overpotentials are likely to occur when increasing the voltage.

Based on our previous experience with the electrodeposition of planar films from the same bath formulation [20], attempts were made to deposit coatings featuring similar Ni/Cu ratios. Several layers were deposited at low current densities (i.e. low overpotentials) in order to favor the preferential deposition of Cu. Figure 3 (curve *a*) shows a typical galvanostatic (i.e., E-t) curve of a Cu-Ni film deposited at low current density, which contains 34 at% Ni percentage (measured by EDX), and is comparable to the Ni content in the microcolumn grown at a voltage of 7.0 V. However, attempts to deposit films featuring even lower Ni contents in a reproducible manner from the same bath formulation failed. The concentration of the metal sulfate salts in the bath was thus slightly modified in order to promote the deposition of films further enriched in Cu. Figure 3 (curve *b*) shows the E-t curve for the deposition of a Cu-Ni film from a bath with higher [Cu(II)]/[Ni(II)] molar ratio (i.e., molar ratio of 28 instead of 10). In this case, the resulting film showed a lower Ni percentage (i.e., 18 at%), close to the average Ni percentage in the microcolumn deposited at a voltage of 6.5 V. Remarkably, the stabilization potential values obtained in both films (around -0.9 V) are similar to those inferred here for the microcolumns (which are also Cu-rich) and less negative than the ones measured in Ni-rich Cu-Ni films [20]. It is important to notice that compared to the microcolumns, the planar films are silvery-bright and extremely flat. A typical SEM image is shown in the inset of Figure 3, for which a very low surface roughness and high compactness (i.e., absence of porosity) was observed. From X-ray diffraction experiments (not shown), both Cu-rich Cu-Ni films were found to exhibit similar grain sizes, around 40 nm.

The development of porosity in the microcolumns can be explained by the relationship between the supply of ions (i.e., mass transport) and their consumption rates. The supplying rate, s , of Cu and Ni ions in a LECD process can be calculated as:

$$s = J_{\text{diff}} A_{\text{diff}} + J_{\text{mig}} A_{\text{mig}} \quad (\text{Eq.5})$$

where J_{diff} and J_{mig} are the flux of ions related to diffusion and migration, respectively, while A_{diff} and A_{mig} are the corresponding areas. Notice that the natural convection term has been neglected since it has been demonstrated to play a minor role on the overall supply rate [11]. According to experimental investigations and theoretical modeling of pure Cu and Ni microcolumns deposited by LECD, A_{diff} can be well represented by a conical boundary and A_{mig} by a semi-spherical boundary [13,21]:

$$A_{\text{diff}} = 2\pi(r + g) \frac{\frac{D}{2} + r}{2} \quad (\text{Eq. 6})$$

$$A_{\text{mig}} = 2\pi r^2 \quad (\text{Eq. 7})$$

where r is the average radius of the microcolumn, g is the gap between the microanode and the top of the microcolumn and D is the diameter of the microanode. With the values of r ($50 \cdot 10^{-6}$ m), g ($15 \cdot 10^{-6}$ m) and D ($175 \cdot 10^{-6}$ m), A_{diff} and A_{mig} are $2.8 \cdot 10^{-8}$ m² and $1.6 \cdot 10^{-8}$ m², respectively.

J_{mig} and J_{diff} can be calculated as follows:

$$J_{\text{diff}} = -D_i \nabla C_i \quad (\text{Eq. 8})$$

$$J_{\text{mig}} = -\frac{Z_i F}{RT} D_i C_i \nabla \Phi \quad (\text{Eq. 9})$$

where D_i is the diffusion coefficient of the ion in m² s⁻¹; ∇C_i is the concentration gradient; $\nabla \Phi$, the potential gradient; Z_i , the charge of the ion and C_i , the local concentration. At pH = 4.5, the main electroactive species of Cu(II) in the bath are the citrate dimeric copper complexes ($[\text{Cu}_2(\text{Cit})_2\text{OH}]^{3-}$) (Figure 4a), and their coefficient diffusion is $2.1 \cdot 10^{-10}$ m² s⁻¹ [22]. The predominant component of Ni(II) is the hexahydrate $\text{Ni}(\text{OH})_6^{2+}$ (Figure 4b), which has a coefficient diffusion of about $1 \cdot 10^{-9}$ m² s⁻¹ [22]. The only unknown parameter to calculate the flux of ions is the local concentration of the dominant electroactive species. If the potential near the LECD region was known, then the Nernst equation could be applied to determine the corresponding steady state concentration at the local site. However, potential data could be only accurately measured if a reference electrode was located in the vicinity of the LECD microregion. Although the local potential was not measured in this work, we can estimate the flux of ions in two opposite cases in order to compare the differences between the deposition of copper and nickel: (i) C_i is 10 times lower than the bulk concentration (large ∇C_i) and (ii) C_i is close to the bulk concentration (small ∇C_i). The fluxes ascribed to diffusion (Eq. 8) for a strong depletion of ions at the cathode surface -case *i*- would be $8.0 \cdot 10^{-5}$ mol s⁻¹ m⁻² for copper and $9.5 \cdot 10^{-3}$ mol s⁻¹ m⁻² for nickel. Likewise, the flux ascribed to migration at a voltage of 6.5 V (Eq. 9) would give values of $2.3 \cdot 10^{-2}$ mol s⁻¹ m⁻² and 1.8 mol s⁻¹ m⁻² for copper and nickel, respectively. Notice that the rate transport is dominated by migration forces due to the strength of the electrical field in the LECD region [11]. The total supply rate (i.e., migration + diffusion) (Eq. 5) is thus $3.6 \cdot 10^{-10}$ mol s⁻¹ for copper and $2.8 \cdot 10^{-8}$ mol s⁻¹ for nickel. Conversely, if case (ii) is considered, then the total supply rate would increase to $3.0 \cdot 10^{-9}$ mol s⁻¹ for copper and $2.7 \cdot 10^{-7}$ mol s⁻¹ for nickel. In any case, the supply rate for nickel is one to two orders of magnitude larger than for copper. The same trend is obtained at a voltage of 7.0 V. Hence, one would expect that for a LECD process conducted at relatively large voltages (6.5-7.0 V) the supply of Cu(II) species to the electrode is not sufficient to compensate for their consumption by electrochemical reduction [13]. The shortage of $[\text{Cu}_2(\text{Cit})_2\text{OH}]^{3-}$ ions rather than

of $\text{Ni}(\text{OH})_6^{2+}$, together with the presumably low overpotential values during LECD (which preclude the growth of Ni-rich microcolumns), is responsible for the formation of pores in the microcolumns.

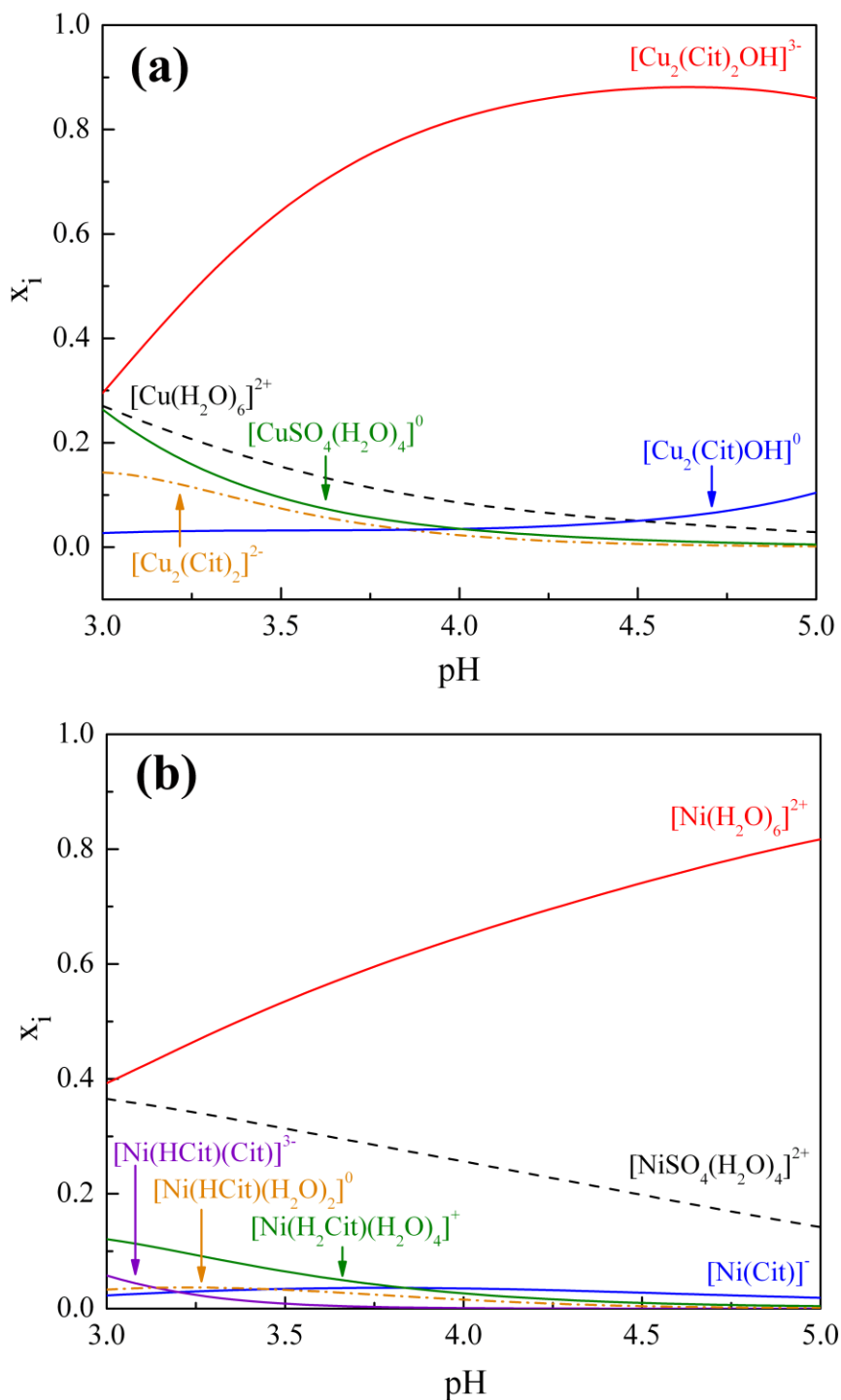


Figure 4. Mole fractions of (a) Cu(II) and (b) Ni(II) species calculated using MEDUSA software as a function of pH for the bath containing 0.7 M $\text{NiSO}_4 \cdot 6\text{H}_2\text{O}$ + 0.025 M $\text{CuSO}_4 \cdot 5\text{H}_2\text{O}$ + 0.3 M $\text{C}_6\text{H}_8\text{O}_7 \cdot \text{H}_2\text{O}$ + $8 \cdot 10^{-4}$ M $\text{NaC}_{12}\text{H}_{25}\text{SO}_4$.

A shortage of Ni(II) species cannot be ruled out, but it is certainly less plausible given that its bulk concentration is 28 times larger than that of copper. Hence, other species present in solution (e.g., protons) are thus likely to be reduced at the expense of Cu(II). The fact that the microcolumns are progressively enriched in nickel along their height also supports the hypothesis that mass transfer of Cu(II) species is strongly hindered. In fact, the charge transfer rate typically exceeds that of mass transport in LECD, the latter being, therefore, the rate-determining process [11].

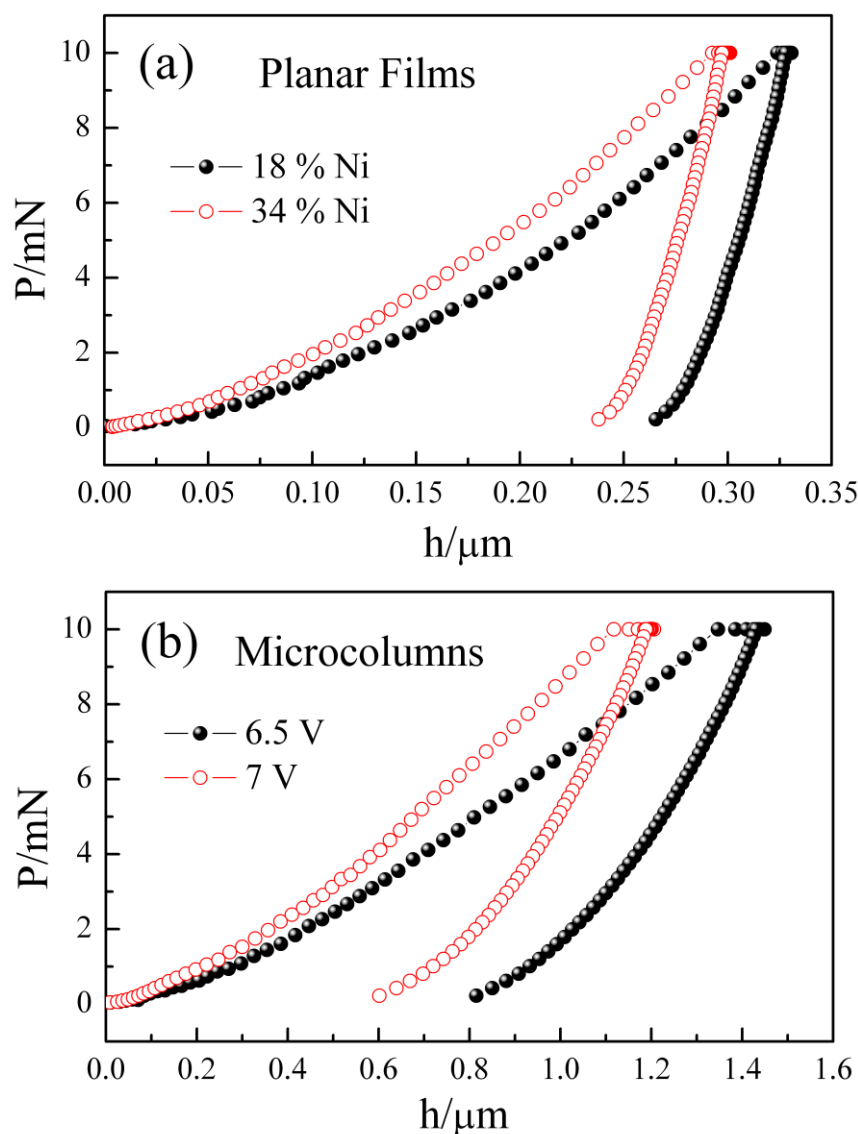


Figure 5. Representative load-displacement indentation curves corresponding to (a) the planar Cu-Ni films with 18 at% and 34 at% Ni and (b) the microcolumns grown using voltages of 6.5 V and 7.0 V.

Representative load-displacement nanoindentation curves for planar Cu-Ni films and microcolumns are shown in Figure 5a and 5b, respectively. For the planar deposits, the maximum penetration depth achieved at the end of the unloading segment decreases as the nickel content in the

film increases. This is an expected result, since copper is intrinsically softer than nickel and the crystallite size in both films was found to be similar. Hence, the film with higher nickel content shows a larger hardness mainly due to solid solution hardening. A similar reasoning explains the differences in Young's modulus between the two films (i.e., the Young's modulus of Cu, $E_{Cu} = 130$ GPa, is lower than that for Ni, $E_{Ni} = 200$ GPa) [23]. A different scenario is found for Cu-Ni microcolumns. First, the hardness values are one order of magnitude lower compared to the 2D deposits (280-470 MPa versus 4-5 GPa). The differences in the Young's modulus between films and microcolumns are even larger. It is clear that these results cannot be explained on the basis of differences in the Ni/Cu ratio between the planar deposits and the microcolumns. Instead, the high porosity level achieved during LECD is likely to play a key role in determining mechanical properties.

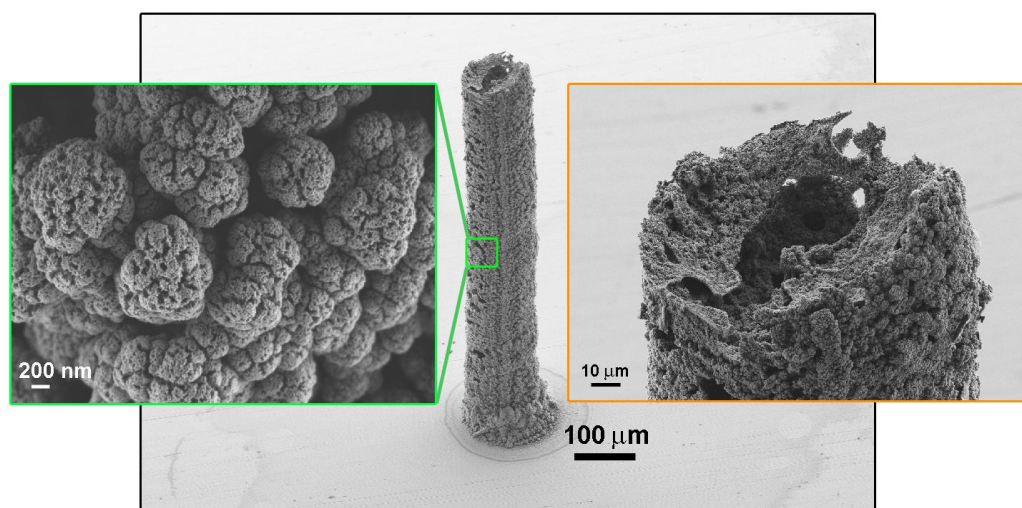


Figure 6. SEM image of a Cu-Ni microcolumn deposited at 7.0 V from a saccharine-free bath. The insets show a detail of the upper part of the microcolumn (right) and a magnified view of the lateral wall (left).

In order to verify the influence of porosity on the nanoindentation results, Cu-Ni microcolumns were produced from saccharine-free baths. It is known that saccharine, as a grain-refining and stress-reliever agent, tends to promote the growth of fully compact nanocrystalline metallic alloys. Hence, the lack of saccharine in the electrolytic bath is likely to cause additional porosity in the microcolumns [24]. Indeed, the resulting microcolumns deposited without saccharine featured higher degree of porosity (cf. Figure 2 and Figure 6). The maximum penetration depth achieved at the end of the unloading segment was larger in this case ($h_{Max} \approx 2.5 \mu\text{m}$), as compared to the microcolumns prepared from the saccharine-containing bath (Fig. 5), indicating that they are mechanically softer. The hardness decreases by about 60% in the absence of saccharine, and the same is true for the E_r values (see Table 1). Although the Cu/Ni ratios were not the exactly same, differences in composition are not sufficient to account for this large variation in H and E_r values.

Our results clearly indicate that H and E_r are strongly influenced by the large degree of porosity that exists in the microcolumns. To a first approximation, while the planar Cu-Ni films can be considered nonporous, the microcolumns may be treated as open-cell metallic foams. In such a case, the Young's modulus, E_{porous} , can be described as follows [25-27]:

$$E_{\text{porous}} = C_1 E_{\text{bulk}} \left(\frac{\rho_{\text{porous}}}{\rho_{\text{bulk}}} \right)^2 \quad (\text{Eq. 10})$$

where E_{bulk} is the Young's modulus of the bulk, nonporous metal (i.e., 140 GPa and 160 GPa, for the Cu-Ni alloys with 18 and 34 at% Ni, respectively), C_1 is a geometry constant close to 1 and $\frac{\rho_{\text{porous}}}{\rho_{\text{bulk}}}$ is the relative density of the foam. From the nanoindentation results (Table 1), and comparing planar films and microcolumns with similar Ni contents, relative densities of around 20.5% and 19.1% can be estimated using Eq. 10 for the microcolumns prepared from the saccharine-containing bath at 6.5 V and 7.0 V, respectively. The relative density further decreases towards values around 14% in Cu-Ni microcolumns prepared from saccharine-free electrolytic baths. These values are twice those reported in the literature for some metallic foams prepared using carbon template approach [25]. These results are in agreement with the pronounced decrease in Young's modulus with the porosity level observed in other families of materials, such as metallic glasses [28], ceramics [29], crystalline metals and metallic alloys [25,26,29,30], silicon [27] or artificial porous rocks [31], measured from nanoindentation experiments and other techniques such as acoustic methods or macroscopic compression tests [25-31].

The decrease of hardness (or compressive yield stress) with porosity is also well documented [24,25,28,29,31] and has been modeled using finite element simulations of nanoindentation curves [33]. A decrease of indentation hardness by more than 50 % has been reported in porous Cu when the relative density reduces from 1 to 0.7 [32]. Nevertheless, while the ratio E/H tends to slightly increase with the porosity level in ceramic materials, the opposite trend is often encountered in metals [26,29]. In our case, E/H decreases from around 35 (in planar films) to approximately 12 (in the microcolumns), thus indicating that the effect of porosity on the Young's modulus is more pronounced than on hardness, which is in agreement with other metallic alloys [29]. It should be noted that when treating the porous microcolumns as open-cell metallic foams, an equation analogous to Eq. 10 may be used to correlate the yield stress of the porous metal with that of the bulk solid material:

$$\sigma_{\text{porous}} = C_2 \sigma_{\text{bulk}} \left(\frac{\rho_{\text{porous}}}{\rho_{\text{bulk}}} \right)^{3/2} \quad (\text{Eq. 11})$$

where $C_2 = 0.3$ [25,26]. Although the relationship between hardness and yield stress in bulk metallic alloys is often taken as $H_{\text{bulk}} \approx 3\sigma_{\text{bulk}}$, a quantitative relationship between hardness and yield stress in porous metals has yet to be established. While some authors consider that the indenter in porous materials is not constrained by the surrounding material regardless of densification (i.e., that the

nanindentation is equivalent to a uniaxial compression test and therefore $H_{\text{porous}} = \sigma_{\text{porous}}$ [25,26], others have shown that, in fact, the relationship between hardness and yield stress in porous metals may still remain the same as for bulk solid alloys, i.e., $H_{\text{porous}} = 3\sigma_{\text{porous}}$ [34,35]. Since the relationship between hardness and compressive yield stress in porous materials remains a controversial issue and, thus, not reliable, the values of Young's modulus, rather than hardness, were used in this work to estimate the relative density of the Cu-Ni microcolumns (see Table 1).

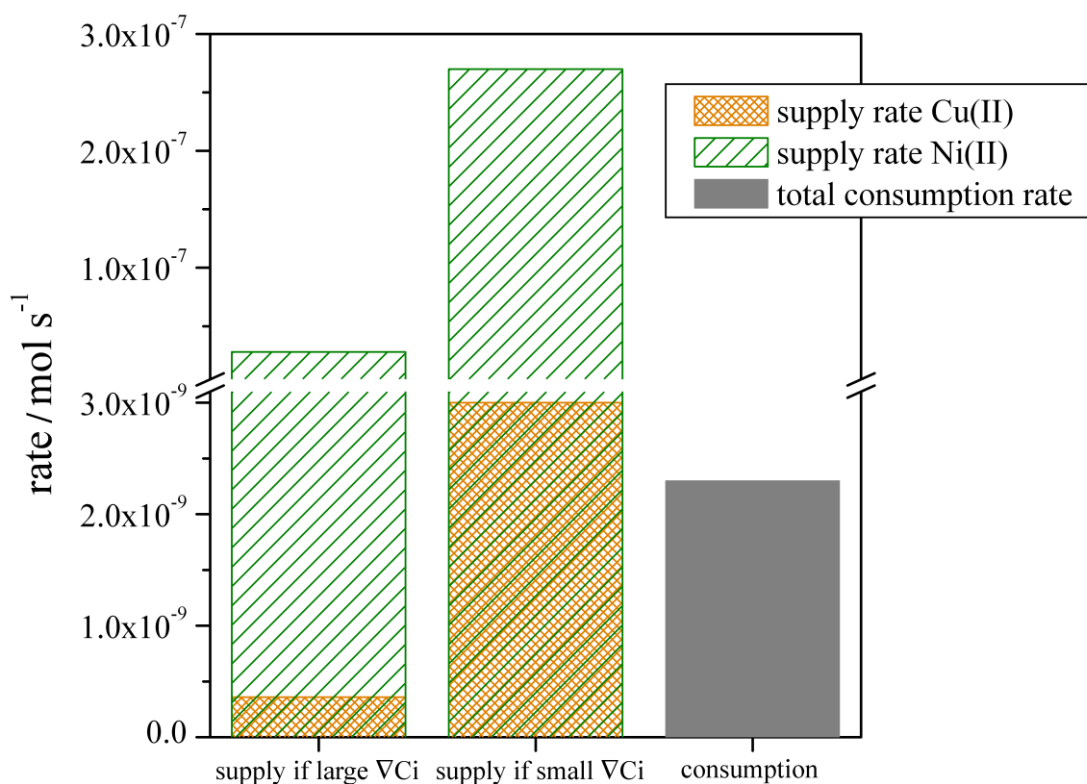


Figure 7. Supply rates for Cu(II) and Ni(II) species and overall consumption rate (i.e., copper + nickel electroreduction) for the microcolumns deposited at 6.5 V from the saccharine-containing bath. For comparison, two opposite cases (for large and small concentration gradients) are considered to calculate the supply rates.

The results from nanoindentation experiments (in particular, the calculated relative density values of the microcolumns) can be used to obtain an estimate of the overall ion consumption rate during the LECD process. The relative density values can be taken as an indirect assessment of the current efficiency, η , of the LECD process:

$$\eta = \frac{W_{\text{actual}}}{W_{\text{theoretical}}} \cong \frac{\rho_{\text{porous}}}{\rho_{\text{bulk}}} \quad (\text{Eq. 12})$$

where W_{actual} and $W_{\text{theoretical}}$ are the actual and theoretical weight deposited, respectively. Then the consumption rate, c , ascribed to Cu and Ni ions electroreduction can be calculated according to the following equation:

$$c = \frac{I\eta}{zF} \quad (\text{Eq. 13})$$

where I is the overall intensity flowed. For η equal to 1, fully compact microcolumns will result. Substituting the values of I (0.0022 A) and η (0.205) for the microcolumns grown at 6.5 V, the resulting consumption rate is of approximately $2.3 \cdot 10^{-9} \text{ mol s}^{-1}$. The overall consumption rate for the microcolumns grown at 7.0 V is nearly the same. In contrast, for the microcolumns deposited from the saccharine-free bath, the overall consumption ratio decreases to $1.2 \cdot 10^{-9} \text{ mol s}^{-1}$. Figure 7 compares the consumption rate with the Cu and Ni supply rates obtained from Eq. 5 for the two cases (large and small ion concentration gradients) at 6.5 V. For the largest concentration gradient considered, the resulting consumption rate would be even lower than the actual value due to the reduced supply of Cu(II) species. Conversely, for the smallest concentration gradient, a higher efficiency and, in turn, a larger consumption rate should be expected given the extra supply of Cu(II) species. The actual supply rate of Cu(II) species would, therefore, fall between the two opposite cases considered for the assessment of supply rates, in order to comply with the consumption rate. These results reinforce the idea that the shortage of copper ions is primarily responsible for the development of porosity in the microcolumns. Secondary reactions like hydrogen co-evolution are expected to take a large percentage of the overall intensity flowed, according to the rather low η values. Hydrogen bubbles originating from proton reduction would cause the observed porosity and rough external appearance of the microcolumns [18]. Notice that although it has been reported that local Joule heating during electrodeposition may cause a temperature increase of 0.5-2 K in the cathode diffuse layer when using low conductive electrolytes in combination with rather large voltages (typically beyond 10 V [36]), such effect can be neglected in the present study, given the conductive nature of the electrolyte. In conventional electroplating and for this type of baths, Cu(II) ions become also depleted as the absolute value of the current density is increased, but the transport rate is still higher than the consumption rate. Indeed, the deposition rate is much lower compared to that in a LECD process, where the electrical field is much stronger. Hence, porosity is not developed but just variations in the Ni/Cu atomic ratio occur. Such variations stem from the fact that copper deposition is mass-transfer controlled while nickel deposition is charge-transfer controlled in citrate-containing solutions [20]. Secondary reactions like hydrogen co-evolution contribute marginally, so that current efficiency is very high.

4. CONCLUSIONS

LECD of Cu-Ni was carried out in order to fabricate Cu-rich alloy microcolumns with large porosity from a citrate-containing solution at voltages of 6.5 and 7.0 V. The mass-transport rates of the predominant Cu(II) and Ni(II) species ($[\text{Cu}_2(\text{Cit})_2\text{OH}]^{3-}$ and $\text{Ni}(\text{OH})_6^{2+}$, respectively, according to bath

speciation) within the LECD microregion have been estimated and compared to the consumption rate due to ion reduction towards the metallic form. Generation of porosity in the microcolumns can be attributed to the strong shortage of Cu(II) species at the brass cathode. The mechanical properties of the fabricated porous microstructures have been compared with those of porous-free Cu-Ni planar layers displaying similar Ni/Cu atomic ratios. The former showed nanoindentation hardness values below 1 GPa and Young's modulus in the range between 3-7 GPa, hence, much lower than in nonporous Cu-Ni alloys. The current efficiency and, in turn, the consumption rate of the LECD process has been estimated from the relative densities (i.e., porosity degree) evaluated by nanoindentation. The present work provides a better understanding on the mechanisms that govern the mass transport kinetics and the electrochemical thermodynamics in the co-deposition of two metals by LECD. In particular, it is demonstrated that the mass-transport equations used to estimate the supply of ions in the LECD of pure Cu and Ni microcolumns can be also successfully applied to the case study of Cu-Ni codeposition. This work also sheds light on the porosity dependence on the mechanical properties in these types of high aspect-ratio microstructures.

ACKNOWLEDGEMENTS

This work has been partially financed by the 2009-SGR-1292 and MAT2011-27380-C02-01 research projects. M.D.B. was partially supported by an ICREA Academia award.

References

1. L. P. Lefebvre, J. Banhart and D. C. Dunand, *Adv. Eng. Mater.*, 10 (2008) 775.
2. W.Y. Zhang, Z.P. Xi, M. Fang, Y.N. Li, G.Z. Li and L. Zhang, *Rare Met. Mater. Eng.*, 37 (2008) 1129.
3. Y. Yamauchi, N. Suzuki, L. Radhakrishnan and L. Wang, *Chem. Record.*, 9 (2009) 321.
4. G. Ryan, A. Pandit and S.P. Apatsidis, *Biomater.*, 27 (2006) 2651.
5. J. Banhart, *Prog. Mater. Sci.*, 46 (2001) 559-U3.
6. J.-H. Kim, R.-H. Kim and H.-S. Kwon, *Electrochem. Commun.*, 10 (2008) 1148.
7. S. Cherevko and C.H. Chung, *Electrochem. Commun.*, 13 (2011) 16.
8. E.N. El Sawy and B.I. Virss, *J. Mater. Chem.*, 19 (2009) 8244.
9. S. Tominaka, T. Momma and T. Osaka, *Electrochim. Acta*, 53 (2008) 4679.
10. Ö.N. Cora, Y. Usta and M. Koç, *J. Micromech. Microeng.*, 19 (2009) 045011.
11. R.A. Said, *Nanotechnology*, 14 (2003) 523.
12. J.H. Yang, J.C. Lin, T.K. Chang, X.B. You and S.B. Jiang, *J. Micromech. Microeng.*, 19 (2009) 02015.
13. J.C. Lin, T.K. Chang, J.H. Yang, Y.S. Chen and C.L. Chuang, *Electrochim. Acta*, 55 (2010) 1888.
14. S. Pané, V. Panagiotopoulou, S. Fusco, E. Pellicer, J. Sort, D. Mochnacki, K.M. Sivaraman, B.E. Kratochvil, M.D. Baró and B.J. Nelson, *Electrochem. Commun.*, 13 (2011) 973.
15. Medusa software by I. Puigdomènech, web site <http://www.kemi.kth.se/medusa/>
16. W.C. Oliver and G.M. Pharr, *J. Mater. Res.*, 7 (1992), 1564.
17. A.C. Fischer-Cripps in: *Nanoindentation* (Ed.: F.F. Ling), Springer, New York, 2004.
18. J.C. Lin, T.K. Chang, J.H. Yang, J.H. Jeng, D.L. Lee and S.B. Jiang, *J. Micromech. Microeng.*, 19 (2009) 015030.
19. J.-C. Lin, T.-K. Chang, J.-H. Yang, Y.-R. Hwang and C. Li in: *Mass Transfer-Advanced Aspects*. (Ed.: H Nakajima), Intech, pp. 207-230.

20. E. Pellicer, A. Varea, S. Pané, B. J. Nelson, E. Menéndez, M. Estrader, S. Suriñach, M. D. Baró, J. Nogués and J. Sort, *Adv. Funct. Mater.*, 20 (2010) 983.
21. T.K. Chang, J.C. Lin, J.H. Hang, P.C. Yeh, D.L. Lee and S.B. Jiang, *J. Micromech. Microeng.*, 17 (2007) 2336.
22. E. Beltowska-Lehman and P. Ozga, *Electrochim. Acta*, 43 (1998) 617.
23. G.V. Samsonov, Handbook of the Physicochemical properties of the Elements, IDI-Plenum, New York, 1968.
24. L. Peraldo Bicelli, B. Bozzini, C. Mele and L. D'Urzo, *Int. J. Electrochem. Sci.*, 3 (2008) 356.
25. D.T. Queheillalt, Y. Katsumura and H.N.G. Wadley, *Scripta Mater.*, 50 (2004) 313.
26. J. Biener, A.M. Hodge, A.V. Hamza, L.M. Hsiung and J.H. Satcher, *J. Appl. Phys.*, 97 (2005) 024301.
27. D. Bellet, P. Lamagnère, A. Vincent and Y. Bréchet, *J. Appl. Phys.*, 80 (1996) 3772.
28. G. Xie, M. Fukuhara, D.V. Louzguine-Luzgin and A. Inoue, *Intermetallics*, 18 (2010) 2014.
29. F. Tancret and F. Osterstock, *Phil. Mag.*, 83 (2003) 125.
30. J.C. Lin, Y.S. Chen, C.F. Huang, J.H. Yang, T.K. Chang, C.-L. Wu, Y.R. Hwang and T.C. Chen, *Int. J. Electrochem. Sci.*, 6 (2011) 3536.
31. M.H. Leite and F. Ferland, *Engng. Geol.*, 59 (2001) 267.
32. H.N. Han, H.S. Kim, K.H. Oh and D.N. Lee, *Powder Metall.*, 37 (1994) 140.
33. S. Carioua, F.-J. Ulma and L. Dormieux, *J. Mech. Phys. Solids*, 56 (2008) 924.
34. H. Li, A. Misra, J. K. Baldwin and S.T. Picraux, *Appl. Phys. Lett.*, 95 (2009) 201902.
35. H.-J. Jin, L. Kurmanaeva, J. Schmauch, H. Rösner, Y. Ivanisenko and J. Weissmüller, *Acta Mater.*, 57 (2009) 2665.
36. P. Barbinschi, *J. Optoelectron. Adv. Mater.*, 8 (2006) 271.